INTERNATIONAL JOURNAL FOR NUMERICAL METHODS IN ENGINEERING
Int. J. Numer. Meth. Engng 2004; **61**:1894–1920
Published online 18 October 2004 in Wiley InterScience (www.interscience.wiley.com). DOI: 10.1002/nme.1138

Bounds for element size in a variable stiffness cohesive finite element model

Vikas Tomar, Jun Zhai and Min Zhou*, †

The George W. Woodruff School of Mechanical Engineering, Georgia Institute of Technology, Atlanta, GA 30332-0405, U.S.A.

SUMMARY

The cohesive finite element method (CFEM) allows explicit modelling of fracture processes. One form of CFEM models integrates cohesive surfaces along all finite element boundaries, facilitating the explicit resolution of arbitrary fracture paths and fracture patterns. This framework also permits explicit account of arbitrary microstructures with multiple length scales, allowing the effects of material heterogeneity, phase morphology, phase size and phase distribution to be quantified. However, use of this form of CFEM with cohesive traction–separation laws with finite initial stiffness imposes two competing requirements on the finite element size. On one hand, an upper bound is needed to ensure that fields within crack-tip cohesive zones are accurately described. On the other hand, a lower bound is also required to ensure that the discrete model closely approximates the physical problem at hand. Both issues are analysed in this paper within the context of fracture in multi-phase composite microstructures and a variable stiffness bilinear cohesive model. The resulting criterion for solution convergence is given for meshes with uniform, cross-triangle elements. A series of calculations is carried out to illustrate the issues discussed and to verify the criterion given. These simulations concern dynamic crack growth in an Al_2O_3 ceramic and in an Al_2O_3/TiB_2 ceramic composite whose phases are modelled as being hyperelastic in constitutive behaviour. Copyright © 2004 John Wiley & Sons, Ltd.

KEY WORDS: cohesive finite element method; element size; dynamic fracture; ceramic composite

1. INTRODUCTION

The cohesive crack approach dates back to the work of Barenblatt [1] for brittle materials and the work of Dugdale [2] for elastoplastic materials. The cohesive finite element method (CFEM) provides a means for quantitative analysis of fracture behaviour through explicit simulation of fracture processes. It has been extensively used to model crack growth in

*Correspondence to: Min Zhou, The George W. Woodruff School of Mechanical Engineering, Georgia Institute of Technology, Atlanta, GA 30332-0405, U.S.A.
†E-mail: min.zhou@me.gatech.edu

Contract/grant sponsor: Army Research Office; contract/grant number: DAAG55-98-1-0454
Contract/grant sponsor: National Science Foundation; contract/grant number: CMS9984298

Received 25 October 2003
Revised 29 December 2003
Accepted 18 May 2004

concrete, ceramics, polymers, composites, and metals. It has also been used to analyse fracture along interfaces. A wide variety of issues have been addressed, including void nucleation (cf. References [3–5]), quasi-static crack growth (cf. References [6–8]), dynamic fracture (cf. References [9–11]), interfacial fracture (cf. References [12–15]), dynamic fragmentation (cf. References [16–19]), dynamic fracture in heterogeneous materials (cf. References [20, 21]), impact-induced delamination in composites (cf. References [22–27]), fracture in polymers, ductile tearing, viscoelastic fracture (cf. References [28–31]), response of ceramics under multi-axial loading (cf. Reference [32]), ductile fracture (cf. References [33–35]), crack growth in functionally graded materials (cf. Reference [36]), and crack propagation in quasi-brittle materials like concrete (cf. Reference [37]). Recent developments include virtual internal bond method [38] for studying fracture at the nano scale, cf. Reference [39]. A discussion of recent improvements in numerical implementation of cohesive zone models is given by de Borst [40] and Planas *et al.* [41].

There are two approaches to analysing fracture using the CFEM when a crack path is unknown in advance. One is to insert cohesive elements into the model as fracture develops (cf. e.g. [42–44]). This approach is effective and extensively used and avoids the issue of cohesive-surface-induced stiffness reduction of the overall model if the traction–separation relation has finite initial stiffness. However, it requires the use of specific fracture initiation criteria that are extrinsic to the constitutive model of the material. In addition, it may be computationally intensive since it involves adaptive meshing at the tip of an advancing crack. The other approach is to embed cohesive surfaces along all finite element boundaries as part of the physical model (cf. References [9, 20, 21]). The additional discretization allows the cohesive surfaces to permeate the whole microstructure as an intrinsic part of the material characterization. The inclusion of cohesive surfaces along all element boundaries over an area in 2D or a volume in 3D allows fracture paths and fracture patterns to be predicted. It assigns a much desired attribute to micromechanical models—the ability to predict fracture pattern and fracture outcome without computational checking at each time step as to which branch of material model to follow in a specific material location. We follow the second approach in our analysis. The finite element mesh used in our analysis has a uniform structure with 'cross-triangle' elements of equal dimensions arranged in a quadrilateral pattern. This type of triangulation is used since it gives the maximum flexibility for resolving crack extensions and arbitrary fracture patterns. The uniform mesh used here avoids the problem of cracks not being able to follow straight paths seen in irregular and non-uniform meshes (cf. Reference [45]). Such uniform meshes are preferable for mixed mode fracture, as pointed out by Scheider and Brocks [33]. In addition, they also minimize mesh-induced dispersion effects in stress wave propagation, cf. Reference [46].

Various traction–separation relations for cohesive surfaces have been proposed. Among them, bilinear models such as those used by Camacho and Ortiz [16], Ortiz and Pandolfi [47], and Espinosa *et al.* [25] and potential relations based on those used by Needleman [3], Tvergaard and Hutchinson [8] and Xu and Needleman [9] are popular, due to their simplicity and straightforward physical background. Carpinteri *et al.* [48] recently proposed a fractal cohesive crack model based on a renormalization group approach for predicting the size effect observed in a wide range of experimental data. In this paper, we present a variable stiffness, bilinear cohesive model for analysing fracture processes in multi-phase microstructures under conditions of plane strain. The primary interest is to provide explicit account of both arbitrary fracture patterns and arbitrary microstructural morphologies. The initial stiffness of the cohesive surfaces

is characterized by an independent parameter, therefore the initially rigid bilinear relation law (cf. e.g. Reference [16]) can be regarded as a special case of the model considered here. The choice of a cohesive law which admits finite initial stiffness is based on several considerations. First, it allows us to consider complicated multiple phase microstructures and still keep the analysis tractable. Second, recent nanoscale simulations of interfacial separation have provided evidence supporting the use of cohesive laws with finite initial stiffness, cf. Reference [49]. At the structural or microscopic scales, the initial slope of the cohesive law may have to do with microcrack behaviour at lower scales, cf. References [50, 51]. Recent asymptotic analyses of mode-I fracture in Reference [52] by coarse graining inter-planar potentials and by determining the corresponding macroscopic cohesive laws for interatomic planes suggest the need of making sure that the overall compliance of the model not be overestimated when traction–separation relations with finite or infinite initial stiffness values are contemplated. Also, it has been found that initially rigid cohesive laws are associated with pathologies in the forms of division by zero (due to the initial infinite slope) and non-convergence in time (due to discontinuities in the traction–separation relation), cf. Reference [53].

For CFEM models with intrinsically embedded cohesive surfaces and cohesive laws with finite initial stiffness, an upper bound on element size must be observed and the stiffness reduction issue due to embedding of cohesive surfaces must be limited or eliminated, cf. References [46, 54]. Specifically, the element size must be small enough to accurately resolve the stress distribution inside the cohesive zones at crack tips. On the other hand, the cohesive surface contribution to stiffness reduction must be small, such that wave speed in the solid is not affected due to the presence of cohesive surfaces. This imposes a lower bound on the size of the elements. In cases where cohesive laws with initially rigid behaviour are used, numerical analyses have been carried out to ascertain the upper limit on the size of the finite element used such that below this limit results are reproducible for any finite element size, cf. e.g. Reference [22]. Results independent of mesh size have been obtained when the mesh adequately resolves the cohesive zone, cf. References [16, 34]. The lower bound for the finite element size is influenced by the initial stiffness of cohesive relation used. Obviously, it is important to quantify the dependence of the lower bound on the initial stiffness.

The first step in our analysis here involves analytical estimates of the upper and lower bounds on element size through considerations of resolution for cohesive zone field and limit for stiffness reduction. These estimates represent general considerations and are then specialized to the case of an Al_2O_3 ceramic and an Al_2O_3/TiB_2 ceramic composite system. The specialized bounds are verified through numerical calculations and are shown to be more accurate and specific for the materials analysed.

2. PROBLEM FORMULATION

A Lagrangian finite deformation formulation is used to account for the finite strains and rotations in crack tip regions. The independent variables are the position of a material point in the reference configuration $\mathbf{x}$ and time t. Relative to a fixed Cartesian frame $xyz \in \mathbf{R}^3$, a material point initially at $\mathbf{x}$ occupies position $\bar{\mathbf{x}}$ in the current configuration. The displacement and the deformation gradient are $\mathbf{u} = \bar{\mathbf{x}} - \mathbf{x}$ and $\mathbf{F} = \partial\bar{\mathbf{x}}/\partial\mathbf{x}$, respectively. The transient finite

deformation kinetics is specified through the principle of virtual work as

$$\int_V \mathbf{s} : \delta\mathbf{F}\,\mathrm{d}V - \int_{S_{\mathrm{int}}} \mathbf{T}\cdot\delta\boldsymbol{\Delta}\,\mathrm{d}S = \int_{S_{\mathrm{ext}}} \mathbf{T}\cdot\delta\mathbf{u}\,\mathrm{d}S - \int_V \rho\,\frac{\partial^2\mathbf{u}}{\partial t^2}\cdot\delta\mathbf{u}\,\mathrm{d}V \tag{1}$$

where $\mathbf{s} : \delta\mathbf{F} = s^{ij}\delta F_{ji}$ in Cartesian co-ordinates; $\mathbf{s}$ is the first Piola–Kirchoff stress; $\boldsymbol{\Delta}$ is the displacement jump across a pair of cohesive surfaces; V, S_{ext} and S_{int} are the volume, external surface area and internal cohesive surface area, respectively, of the body in the reference configuration. The density of the material in the reference configuration is ρ. $\delta\mathbf{F}$, $\delta\boldsymbol{\Delta}$, and $\delta\mathbf{u}$ denote admissible variations in $\mathbf{F}$, $\boldsymbol{\Delta}$ and $\mathbf{u}$, respectively. The traction vector $\mathbf{T}$ and the surface normal $\mathbf{n}$ in the reference configuration are related through $\mathbf{T} = \mathbf{n}\cdot\mathbf{s}$. The volumetric constitutive law is hyperelastic so that

$$\mathbf{S} = \frac{\partial \mathrm{W}}{\partial \mathbf{E}} \tag{2}$$

where, $\mathbf{S} = \mathbf{s}\cdot\mathbf{F}^{-\mathrm{T}}$ is the second Piola–Kirchoff stress tensor. W is the strain energy density, taken to be

$$\mathrm{W} = \tfrac{1}{2}\mathbf{E} : \mathbf{L} : \mathbf{E} \tag{3}$$

with

$$\mathbf{L} = \frac{E}{1+v}\left(\mathbf{II} + \frac{v}{1-2v}\,\mathbf{I}\otimes\mathbf{I}\right) \tag{4}$$

being the tensor of isotropic elastic moduli. E and v are Young's modulus and Poisson's ratio, respectively. $\mathbf{E}$ is the Lagrangian strain given by

$$\mathbf{E} = \tfrac{1}{2}(\mathbf{F}^{\mathrm{T}}\cdot\mathbf{F} - \mathbf{I}) \tag{5}$$

In the above formulae, $\mathbf{II}$ is the fourth-order identity tensor, $\mathbf{I}$ is the second-order identity tensor, $\mathbf{I}\otimes\mathbf{I}$ denotes the outer product of two second-order tensors, and $()^{\mathrm{T}}$ and $()^{-\mathrm{T}}$ denote transpose and inverse transpose, respectively.

Note that cohesive traction $\mathbf{T}$ applied on material points P and P' coinciding at and occupying position $\mathbf{x}$ on cohesive surface S_0 in the reference configuration is work-conjugate to surface separation $\boldsymbol{\Delta}$. Reckoned in the reference configuration, the cohesive law is

$$\mathbf{T}(\mathbf{x}) = \mathbf{T}[\boldsymbol{\Delta}(\mathbf{x})] \tag{6}$$

and the work of separation under this traction at any stage of deformation is [47]

$$\mathrm{W}_{\mathrm{sep}} = \int_{S_0}\int_0^{\boldsymbol{\Delta}} \mathbf{T}(\mathbf{x})\cdot\mathrm{d}\boldsymbol{\Delta}\,\mathrm{d}S \tag{7}$$

Implied here is the assumption that cohesive traction–separation relations are locally determined, i.e. the cohesive traction at one point is fully determined by the separation at the point itself. A review of various types of cohesive laws is given by, e.g. Reference [55].

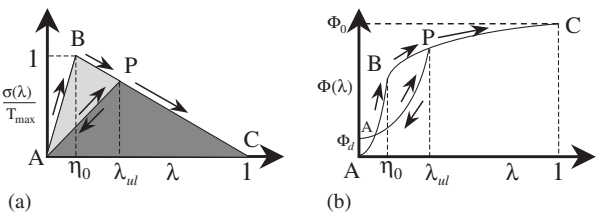

Figure 1. Irreversible bilinear cohesive law.

2.1. Bilinear law

Although the discussion here will focus on tensile loading, compression and contact can be dealt with as well within this framework, cf. Reference [56]. The bilinear law used can be regarded as a generalized version of those with irreversibility given by Camacho and Ortiz [16] and Ortiz and Pandolfi [47]. However as in Reference [25], we have an additional parameter to account for the finite initial stiffness of the cohesive surfaces. Further, the current law is derived from a potential Φ which is a function of separation vector Δ through a state variable defined as $\lambda = \sqrt{(\Delta_{\mathrm{n}}/\Delta_{\mathrm{nc}})^2 + (\Delta_{\mathrm{t}}/\Delta_{\mathrm{tc}})^2}$. This variable describes the effective instantaneous state of mixed-mode separations. Here, $\Delta_{\mathrm{n}} = \mathbf{n} \cdot \boldsymbol{\Delta}$ and $\Delta_t = \mathbf{t} \cdot \boldsymbol{\Delta}$ denote, respectively, the normal and tangential components of Δ, with $\mathbf{n}$ and $\mathbf{t}$ being unit vectors normal and tangent to S_0, respectively. Δ_{nc} is the critical normal separation at which the cohesive strength of an interface vanishes under conditions of pure normal deformation ($\Delta_{\mathrm{t}} = 0$). Similarly, Δ_{tc} is the critical tangential separation at which the cohesive strength of an interface vanishes under conditions of pure shear deformation ($\Delta_{\mathrm{n}} = 0$). λ tracks instantaneous mixed-mode separations during both loading and unloading. Clearly, $\lambda = 0$ corresponds to $\boldsymbol{\Delta} = \mathbf{0}$ (undeformed state or fully unloaded state) and $\lambda \geqslant 1$ implies complete separation, i.e. total debonding of the cohesive surface pair.

In order to account for the irreversibility of separations, a parameter $\eta = \max\{\eta_0, \lambda_{\mathrm{ul}}\}$ is defined. As illustrated in Figure 1(a), η_0 is the initial value of η which defines the stiffness of the original undamaged cohesive surface and λ_{ul} is the hitherto maximum value of λ *at which an unloading process was initiated*. Note that λ_{ul} is associated with the onset of an unloading event and is not necessarily the hitherto maximum value of λ. Obviously, λ_{ul} represents the (reduced) current stiffness of the cohesive surfaces after damage and unloading have occurred. Also, one always has $\eta < 1$. While η_0 is the characteristic value of effective separation λ at which the effective traction σ (see below) for a cohesive surface pair reaches the strength $T_{\max}$ of the undamaged surface, λ_{ul} is the critical level of λ at which σ reaches the reduced strength $T_{\max}(1-\eta)/(1-\eta_0)$ of the hitherto damaged cohesive surface pair.

The specific form for the potential is taken as

$$\Phi = \Phi(\lambda, \eta) = \begin{cases} \Phi_0 \left(\dfrac{1-\eta}{1-\eta_0}\right)\left(\dfrac{\lambda^2}{\eta}\right) & \text{if } 0 \leqslant \lambda \leqslant \eta \\ \Phi_0 \left(\dfrac{1-\eta}{1-\eta_0}\right)\left(1 - \dfrac{(1-\lambda)^2}{1-\eta}\right), & \text{if } \eta < \lambda \leqslant 1 \end{cases} \tag{8}$$

This relation allows the traction to be defined through

$$\mathbf{T} = \frac{\partial \Phi}{\partial \boldsymbol{\Delta}} \tag{9}$$

yielding the normal and shear traction components as

$$T_{\mathrm{n}} = \sigma(\lambda, \eta)\frac{\Delta_{\mathrm{n}}}{\lambda \Delta_{\mathrm{nc}}} \quad \text{and} \quad T_{\mathrm{t}} = \sigma(\lambda, \eta)\frac{\alpha \Delta_{\mathrm{t}}}{\lambda \Delta_{\mathrm{tc}}} \tag{10}$$

In the above expressions, $\alpha = \Delta_{\mathrm{nc}}/\Delta_{\mathrm{tc}}$ and

$$\sigma = \sqrt{(T_{\mathrm{n}})^2 + (T_{\mathrm{t}}/\alpha)^2} = \begin{cases} \left(T_{\max}\dfrac{1-\eta}{1-\eta_0}\right)\dfrac{\lambda}{\eta} & \text{if } 0 \leqslant \lambda \leqslant \eta \\ \left(T_{\max}\dfrac{1-\eta}{1-\eta_0}\right)\dfrac{1-\lambda}{1-\eta} & \text{if } \eta < \lambda \leqslant 1 \\ 0 & \text{if } \lambda > 1 \end{cases} \tag{11}$$

For a surface that has previously been deformed to $\lambda = \eta$ and has experienced unloading from this value of λ, the work of separation for an arbitrary separation process is (see Equations (8) and (9))

$$\int_0^{\Delta_{\mathrm{c}}} \mathbf{T} \cdot \mathrm{d}\boldsymbol{\Delta} = \Phi(1, \eta) \tag{12}$$

where Δ_{c} is the critical separation under general mixed mode conditions at which σ vanishes and by definition $\lambda(\Delta_{\mathrm{c}}) = 1$. In particular, for pure normal separations $\Delta_{\mathrm{c}} = \{\Delta_{\mathrm{nc}}, 0\}$ and for pure tangential separations $\Delta_{\mathrm{c}} = \{0, \Delta_{\mathrm{tc}}\}$. Since the unloading and reloading along AP (Figure 1(a)) are fully elastic, the amount of work required to fully separate a unit surface area from the undamaged state is

$$\int_0^{\Delta_{\mathrm{c}}} \mathbf{T} \cdot \mathrm{d}\boldsymbol{\Delta} = \Phi(1, \eta_0) = \Phi_0 \tag{13}$$

This constant can be calibrated through pure normal and pure shear separations, i.e.

$$\begin{aligned} \Phi_0 &= \int_0^{\Delta_{\mathrm{nc}}} T_{\mathrm{n}}\,\mathrm{d}\Delta_{\mathrm{n}} = \int_0^{\eta_0\Delta_{\mathrm{nc}}} \left(T_{\max}\frac{\Delta_{\mathrm{n}}}{\eta_0\Delta_{\mathrm{nc}}}\right)\mathrm{d}\Delta_{\mathrm{n}} + \int_{\eta_0\Delta_{\mathrm{nc}}}^{\Delta_{\mathrm{nc}}} \left(T_{\max}\frac{1-\frac{\Delta_{\mathrm{n}}}{\Delta_{\mathrm{nc}}}}{1-\eta_0}\right)\mathrm{d}\Delta_{\mathrm{n}} \\ &= \int_0^{\Delta_{\mathrm{tc}}} T_{\mathrm{t}}\,\mathrm{d}\Delta_{\mathrm{t}} = \int_0^{\eta_0\Delta_{\mathrm{tc}}} \left(T_{\max}\frac{\alpha\Delta_{\mathrm{t}}}{\eta_0\Delta_{\mathrm{tc}}}\right)\mathrm{d}\Delta_{\mathrm{t}} + \int_{\eta_0\Delta_{\mathrm{tc}}}^{\Delta_{\mathrm{tc}}} \left(\alpha T_{\max}\frac{1-\frac{\Delta_{\mathrm{t}}}{\Delta_{\mathrm{tc}}}}{1-\eta_0}\right)\mathrm{d}\Delta_{\mathrm{t}} \\ &= \frac{1}{2}\,T_{\mathrm{n}}^{\max}\Delta_{\mathrm{nc}} = \frac{1}{2}\,\alpha T_{\mathrm{n}}^{\max}\Delta_{\mathrm{tc}} \end{aligned} \tag{14}$$

Apparently, $T_{\max} = T_{\mathrm{n}}^{\max}$ is the maximum cohesive traction under conditions of pure normal separation.

While the bilinear relationship between σ and λ embodied in the above formulation is illustrated in Figure 1(a), the variation of Φ is shown in Figure 1(b). Overall, five parameters are needed to specify the cohesive behaviour, including the maximum tensile strength $T_{\max}$, the critical separations Δ_{nc} and Δ_{tc}, characteristic separation η_0, and α. Note that only four of these parameters are independent since $\alpha = \Delta_{\mathrm{nc}}/\Delta_{\mathrm{tc}}$. The calibration of these parameters is an important aspect in the implementation of the CFEM model. $T_{\max}$ is commonly assumed to be a fraction of the Young's modulus, cf. e.g. Reference [9]. The critical separations Δ_{nc} and Δ_{tc} are usually obtained by equating the area under the cohesive relation to the formation energy per unit area of the corresponding fracture surface. In this regard, experimental efforts have been reported, cf. e.g. References [51, 57]. The value of α is typically obtained from the ratio between the tangential and normal energy release rates, cf. e.g. Reference [25]. In this paper, the approach in Reference [9] is used.

Equation (11) describes a two-stage behaviour as illustrated in Figure 1. Between A and B ($0 \leqslant \lambda \leqslant \eta_0$), separation occurs elastically and the cohesive energy stored (work done in causing separation) is fully recoverable. Damage in the form of microcracks and other small-scale defects does not occur. Between B and C ($\eta_0 \leqslant \lambda \leqslant 1$), material degradation causes progressive reduction in the strength of the cohesive surfaces. This represents a phenomenological account of the effects of microcracks and other defects not explicitly modelled in the CFEM framework. Unloading from any point P follows path PA and subsequent reloading follows AP and then PC. Part of the work expended on causing the separation in this regime is irrecoverable, as indicated by the hysteresis loop ABP which implies dissipation during the softening process. Correspondingly, there is a decrease in the maximum tensile strength of the cohesive surface. This is reflected in the elastic reloading of the interface along AP and further softening along path PC. To correctly account for this behaviour, it is necessary to record the value of λ_{ul}. We must point out that the dependence of the damaged behaviour on previous deformation is very weak and limited, only through η which tracks the hitherto largest extend of separation from which unloading has occurred. Any other aspect of preceding loading–unloading cycles does not in any way influence the deformation. This behaviour is similar to the Markov chain (cf. e.g. Reference [58]) in stochastic analyses.

Since any unloading and reloading (along PA in Figure 1(a) or PA$'$ in Figure 1(b)) are elastic, the amount of work that has been dissipated is

$$\Phi_{\mathrm{d}}(\lambda,\eta) = \begin{cases} 0 & \text{if } \lambda \leqslant \eta_0 \\ \Phi(\eta,\eta_0) - \Phi(\eta,\eta) = \dfrac{\eta-\eta_0}{1-\eta_0}\,\Phi_0 & \text{if } \eta_0 < \lambda \leqslant \eta \\ \Phi(\lambda,\eta_0) - \Phi(\lambda,\eta) = \dfrac{\lambda-\eta_0}{1-\eta_0}\,\Phi_0 & \text{if } \eta < \lambda \leqslant 1 \\ \Phi_0 & \text{if } \lambda > 1 \end{cases} \tag{15}$$

Note here that $\eta_0 < \eta = \max\{\eta_0, \lambda_{\mathrm{ul}}\} < 1$ and that η never attains the value of 1. The dissipation is uniquely defined and $\Phi_{\mathrm{d}}(\lambda,\eta)$ is a monotonically increasing function. When full separation is achieved, $\Phi_{\mathrm{d}}(1,\eta) = \Phi_0 \cdot \Phi_{\mathrm{d}}$ is partly converted into the surface energy and partly spent on causing damage in the material adjacent to crack surfaces through microcrack formation not explicitly modelled. A unique damage parameter can be defined to phenomenologically track the

progressive softening of cohesive surfaces interspersed throughout the composite microstructure. This parameter D is defined such that

$$D = \frac{\Phi_{\mathrm{d}}}{\Phi_0} \tag{16}$$

Note that $0 \leqslant D \leqslant 1$, with $D = 0$ indicating fully recoverable interfacial separation and $D = 1$ signifying complete separation or total fracture. In the numerical analysis carried out in References [59, 60], D is used as a state variable quantifying the degree of the damage, providing a phenomenological measure for failure analysis. The spatial and time variation of $D = D(\mathbf{x}, t)$ allows the distribution and evolution of damage in various microstructures to be analysed. Finally, it is important to remember that the development in this section is different from the interfacial cohesive laws for fatigue by Nguyen *et al.* [61], as reloading here follows the same path (AP in Figure 1(a)) as unloading.

A well-posed initial/boundary value problem consists of constitutive equations of materials, appropriate field equations, initial and/or boundary conditions. In general, the field equations appear as partial differential equations. Finite element discretization of field equations for the model with cohesive surfaces leads to a system of differential algebraic equations that can be solved numerically.

2.2. *Finite element discretization*

The finite element discretization of Equation (1) leads to a system of linear algebraic equations of the form

$$\mathbf{M}\frac{\partial^2 \mathbf{U}}{\partial t^2} = -\mathbf{R} \tag{17}$$

where, $\mathbf{U}$ is the vector of nodal displacements, $\mathbf{M}$ is the nodal mass matrix and $\mathbf{R}$ is the nodal force vector consisting of contributions from both the bulk elements and the cohesive surfaces, i.e. $\mathbf{R} = \mathbf{R}^{\mathrm{b}} + \mathbf{R}^{\mathrm{c}}$, where $\mathbf{R}^{\mathrm{b}} = \int_V \mathbf{B}^{\mathrm{T}}\mathbf{s}\,\mathrm{d}V$ and $\mathbf{R}^{\mathrm{c}} = \int_{S_{\mathrm{int}}} \mathbf{N}^{\mathrm{T}}\mathbf{T}\,\mathrm{d}S$ denote the force vector contributions from bulk elements and cohesive surfaces, respectively. Here, $\mathbf{N}$ denotes the finite element shape function and $\mathbf{B}$ is the spatial gradient of $\mathbf{N}$. Krieg and Key [62] showed that from the point of view of accuracy as well as computational efficiency a lumped mass matrix is preferable for explicit time integration procedures. Therefore, a lumped mass matrix $\mathbf{M}$ is used in Equation (17) instead of the consistent mass matrix. The explicit time-integration scheme based on the Newmark β-method with $\beta = 0$ and $\gamma = 0.5$ is employed to integrate Equation (17), cf. Reference [63]. The displacements and velocities at $t_{n+1} = t_n + \Delta t_n$ are obtained by integrating the equations of motion using Newmark β-method as

$$\begin{aligned} \frac{\partial^2 \mathbf{U}^{n+1}}{\partial t^2} &= \mathbf{M}^{-1}\mathbf{R} \\ \frac{\partial \mathbf{U}^{n+1}}{\partial t} &= \frac{\partial \mathbf{U}^{n}}{\partial t} + \frac{1}{2}\Delta t_n \left(\frac{\partial^2 \mathbf{U}^{n+1}}{\partial t^2} + \frac{\partial^2 \mathbf{U}^{n}}{\partial t^2} \right) \end{aligned} \tag{18}$$

and

$$\mathbf{U}^{n+1} = \mathbf{U}^n + \Delta t_n \frac{\partial \mathbf{U}^n}{\partial t} + \frac{1}{2}(\Delta t_n)^2 \frac{\partial^2 \mathbf{U}^n}{\partial t^2}$$

where $(\bullet)^{-1}$ denotes the matrix inverse. The time increment is taken to be Δt. The magnitude of Δt is based on the Courant–Freidrichs–Lewy criterion and material-related numerical stability considerations for explicit time integration. Another factor influencing the time step is the cohesive separation process. Specifically in the current work, the time step Δt also needs to be small enough to ensure that the increment of the cohesive separation Δ (or $\Delta\lambda$) be sufficiently small in each numerical step to avoid numerical instability. An empirical criterion of $\Delta\lambda < 0.05\eta$ is used, see Reference [21]. In the calculations carried out here for Al_2O_3, the typical average time step is on the order of 1 ps which is approximately $\frac{1}{200}$ of the time it takes for the longitudinal wave to traverse the smallest bulk element. This time step value is significantly smaller than that in FEM calculations without cohesive surfaces. Clearly, the cohesive separation process brings about a significant increase in computational cost.

3. ELEMENT SIZE INDEPENDENCE: THEORETICAL BOUNDS

At least three primary length scales are operative in a CFEM model, including the specimen dimension (L), grain/inclusion size (d_g), and mesh size h. We assume that the length scales associated with grains, inclusions, and specimen geometry constitute long range contributions to deformation and their effect on the choice of local element size is relatively small. This is a reasonable assumption since elements must be significantly smaller than most of these length scales (e.g. $h \ll L$ and $h \gg d_g$) in order to obtain an accurate resolution of fields near crack-tips. In addition to the usual requirements for elements in regular FEM models, two other factors influence the element size independence and reproducibility of solutions in CFEM. The first factor is the cohesive zone size (d_z). The element size must be small enough ($h \ll d_z$) to accurately resolve the stress distribution in cohesive zones at crack tips. The cohesive zone size is an inherent length scale determined by material properties. It is the smallest physical length in most cases. The second factor results from the macroscopic stiffness reduction due to cohesive separation along element boundaries if the initial stiffness of cohesive surfaces is finite. The element size must be chosen to prevent excessive stiffness reduction or change in the overall characteristics of CFEM models. The later issue is specific to CFEM models that contain cohesive surfaces along all element boundaries and use cohesive laws with finite initial stiffness. These two issues are addressed in the forthcoming sections to obtain a range of element size that ensures the element size-independence and convergence of CFEM solutions.

3.1. Cohesive zone size

The high stress and strain gradients in crack tip regions necessitate the use of very fine meshes. The fracture process zones involve large plastic deformations and/or microcrack/microvoid formation. The cohesive zone model, introduced by Barenblatt [1] and Dugdale [2], characterizes a fracture process zone as a cohesive zone in which cohesive traction is related to face separation in the prospective fracture surfaces ahead of a crack tip. The relationship between the cohesive force and separation varies, depending on mechanisms as well as material properties,

cf. Reference [64]. The size of a cohesive zone is determined from a boundedness condition for removing stress singularity at the crack tip. This size sets one of the length scales in CFEM models. Clearly, finite element meshes must be fine enough to resolve details of the deformation fields around crack tips and the traction distributions inside cohesive zones. Planas and Elices [65] analysed the asymptotic growth of a cohesive crack in a strain softening material with the objective of studying mode-I crack growth in structures. A zeroth-order analysis of the near- and far-field of cohesive crack models predicted that the mode-I critical cohesive zone size has the lower bound such that

$$d_z \geqslant \frac{\pi}{32}\,\Delta_c^2\,\frac{E'}{G_{IC}} \tag{19}$$

Here, $E' = E$ for plane stress and $E' = E/(1-\nu^2)$ for plane strain. G_{IC} denotes the critical mode-I strain energy release rate. Δ_c is the crack tip opening displacement at the location where the traction across a pair of cohesive surfaces becomes zero. The lower bound in Equation (19) is applicable to an arbitrary cohesive law provided that the specimen size is very large compared with the size of the cohesive zone. For Dugdale type cohesive laws which assume that the cohesive stress T_{max} is a constant equal to the yield stress of the material, the cohesive zone size for mode-I under plane strain conditions is Reference [64]

$$d_z = \frac{\pi}{8}\,\frac{E}{1-\nu^2}\,\frac{G_{IC}}{T_{max}^2} \tag{20}$$

For cracks with cohesive relations that can be derived from a potential such as the one in Equation (8), Reference [66], the cohesive zone size can be further written as

$$d_z = \frac{9\pi}{32}\,\frac{E}{(1-\nu^2)}\,\frac{\Phi_0}{T_{max}^2} \tag{21}$$

Camacho and Ortiz [16] used Equation (20) in their analysis on element size which concerns mode-I crack propagation. Since we focus on mixed mode conditions, Equation (21) is more appropriate for the analysis here. We require that the characteristic element size satisfy $h \ll d_z$.

3.2. Cohesive surface induced stiffness reduction

Cohesive surfaces contribute to the overall deformation of the specimen. For CFEM models that include cohesive surfaces along all element boundaries as an intrinsic component, the density of the cohesive surfaces (cohesive surfaces area per unit volume) increases as elements are refined. The increase in cohesive surface density causes the overall deformation to increase without an increase in applied loading if the initial stiffness of cohesive surfaces is finite. This increase in compliance or decrease in stiffness of the overall model represents a change in the property of the model. It causes the solution to diverge due to the changing characteristics of the model. The effect of this issue is negligible when cohesive surfaces are only specified along a potential single crack path such as the case in Reference [67] or if the initial stiffness of cohesive surfaces is infinite. The effects of this issue on the solution must be minimized. Several methods can be used to achieve this objective. For example, the stiffness of the bulk elements can be increased to compensate for the stiffness reduction due to interfacial separation. Another approach is to limit the density of the cohesive surfaces in a model. This requires that a lower limit be set for the finite element size. The effects of both approaches are discussed

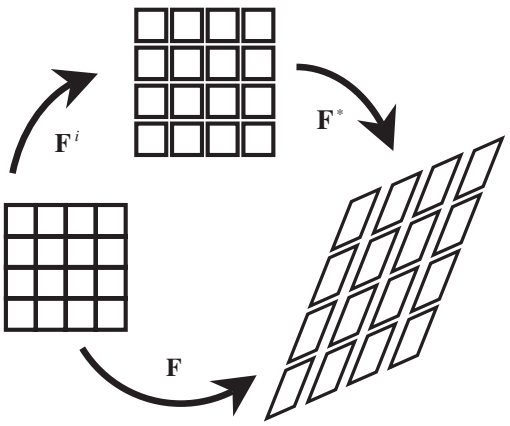

Figure 2. A schematic illustration of deformation decomposition in CFEM.

in this paper and the criterion we develop here specifies the minimum allowable element size as a function of a number of factors, including the attributes of the cohesive law and the bulk constitutive law in the model. The minimum allowable element size also depends on the geometry of the meshes used. Before an estimate of this lower limit can be obtained, an analysis of the overall deformation accounting for both bulk straining and interfacial separation is in order.

An illustration of the bulk element-cohesive interface model is shown Figure 2. For the continuum represented by the aggregate of bulk elements and cohesive surfaces, the overall macroscopic deformation gradient $\mathbf{F}$ comprises two parts which result from bulk material deformation and cohesive surface separation, respectively. Specifically

$$\mathbf{F} = \mathbf{F}^*\mathbf{F}^i \tag{22}$$

where $\mathbf{F}$ is the overall macroscopic deformation gradient, $\mathbf{F}^*$ accounts for the contribution from bulk deformation within elements, and $\mathbf{F}^i$ accounts for the effect of separation along cohesive surfaces. The overall strain $\mathbf{E}$ and the strain in the bulk elements $\mathbf{E}^*$ are, respectively,

$$\mathbf{E} = \tfrac{1}{2}\,(\mathbf{F}^{\mathrm{T}}\mathbf{F} - \mathbf{I})$$

and

$$\mathbf{E}^* = \mathbf{L}^{-1} : \mathbf{S} \tag{23}$$

where, $\mathbf{L}^{-1}$ is the material compliance tensor and $\mathbf{S}$ is the second Piola–Kirchhoff stress tensor. The deformation gradient accounting for cohesive separations can be expressed as

$$\mathbf{F}^i = \mathbf{I} + \frac{1}{V}\int_{S_{\mathrm{int}}} \boldsymbol{\Delta} \otimes \mathbf{n}\,\mathrm{d}S \tag{24}$$

where V is a representative volume over which the contribution of cohesive surfaces to deformation is averaged. The above relation is a volume-averaged measure of the contribution of Δ

to deformation gradient. This representation is obvious if one considers uniform deformation with evenly spaced, parallel cohesive surfaces. The corresponding Lagrangian strain can be expressed as

$$\mathbf{E}^i = \tfrac{1}{2}(\mathbf{F}^{i^{\mathrm{T}}}\mathbf{F}^i - \mathbf{I}) \tag{25}$$

In order for the overall discrete model to approximate the original continuum, the contribution to the overall strain by $\mathbf{F}^i$ must be small compared with the contribution by $\mathbf{F}^*$, i.e.

$$\|\mathbf{E}^i\| \ll \|\mathbf{E}^*\| \tag{26}$$

where, $\|\|$ denotes an appropriate norm. In a CFEM model, $\|\mathbf{E}^i\|$ varies with the geometric size and arrangement of elements. Thus, estimates of $\|\mathbf{E}^i\|$ can only be obtained for specific CFEM configurations. A relative increase in compliance can be defined as

$$R = \frac{\|\mathbf{E}^i\|}{\|\mathbf{E}^*\|} = \frac{\|\mathbf{E}^i\|}{\|\mathbf{L}^{-1} : \mathbf{S}\|} = \frac{\|\mathbf{L}_{\mathrm{eff}}^{-1} : \mathbf{S} - \mathbf{L}^{-1} : \mathbf{S}\|}{\|\mathbf{L}^{-1} : \mathbf{S}\|} \approx \frac{\|\mathbf{L}_{\mathrm{eff}}^{-1} - \mathbf{L}^{-1}\|}{\|\mathbf{L}^{-1}\|} \tag{27}$$

$\mathbf{L}_{\mathrm{eff}}$ is the tensor of effective moduli of the model with cohesive surfaces and can be written as

$$L_{\mathrm{eff}} = \frac{E_{\mathrm{eff}}}{1+v}\left(\mathbf{II} + \frac{v_{\mathrm{eff}}}{1-2v_{\mathrm{eff}}}\,\mathbf{I}\otimes\mathbf{I}\right) \tag{28}$$

Here, E_{eff} is the effective Young's modulus and v_{eff} is the effective Poisson's ratio. Clearly, to ensure that the overall response of a CFEM model remains substantially similar to that of the original system, we must require that $R \ll 1$. $\mathbf{F}^i$ and $\mathbf{E}^i$ are dependent on the size and shape of the elements used. Since the calculations in this paper, in References [59, 60] use meshes with 'cross-triangle' elements arranged in a quadrilateral pattern analyses here concern only this type of element design. Although the relations so obtained may not be used directly for meshes with other geometric designs, the general trend and the parameter dependence should hold true in general.

The discrete approximation of a continuum with cohesive surfaces and bulk elements causes the response of the element-interface aggregate to be anisotropic in general. However, since the interest is to obtain a close approximation of the material behaviour we focus on the effective properties of the cohesive surface and bulk element aggregate. Within the hyperelastic constitutive framework of Equations (3) and (4), we surmise the existence of a relation among the effective Young's modulus E_{eff}, effective Poisson's ratio v_{eff} and effective shear modulus of the form of $G_{\mathrm{eff}} = \{E_{\mathrm{eff}}/2(1+v_{\mathrm{eff}})\}$. Under this condition, the effective properties of a CFEM model are loading-mode dependent because of the discrete nature of the model and because of the differing responses of cohesive surfaces to mode-I and mode-II loading. To account for the differing responses to different stress states, deformations under three fundamental loading modes (uniaxial tension, biaxial tension and pure shear) are analysed and the relative increase in compliance R in each case is obtained. These three fundamental loading modes are chosen such that they cover the complete range of loading modes consistent with two-dimensional mixed mode fracture. The lower bound for element size is then determined by using the largest R among the values obtained. It is important to note that such an analysis allows the basic parametric dependence and the quantitative scale of stiffness changes to be characterized. The analysis is not meant to produce absolute bounds for the relative increase in compliance, nor is

such a pursuit necessary. To simplify the analysis, uniform stress field is assumed in all cases. Also, plane stress/strain conditions are assumed to prevail. Derivations of the effective moduli for the three loading modes considered are given in the appendix. The corresponding relative increases in compliances are

$$R_1 = \frac{1/E_{\text{eff}} - 1/E'}{1/E'} = \frac{E'}{h}\left(\frac{\eta_0\Delta_{\text{tc}}}{T_{\max}}\right)\left[\left(\frac{\sqrt{2}+2}{2}\right)\alpha + \frac{\sqrt{2}}{2\alpha}\right]$$

$$R_2 = \frac{(1-\nu_{\text{eff}})/E_{\text{eff}} - (1-\nu)/E'}{(1-\nu)/E'} = \frac{E'}{(1-\nu)h}\left(\frac{\eta_0\Delta_{\text{tc}}}{T_{\max}}\right)\left[\frac{\sqrt{2}}{\alpha} + \alpha\right]$$

and

$$R_3 = \frac{1/G_{\text{eff}} - 1/G}{1/G} = \frac{G}{h}\left(\frac{\eta_0\Delta_{\text{tc}}}{T_{\max}}\right)\left[\frac{2}{\alpha} + 2\sqrt{2}\alpha\right] \tag{29}$$

Here, h is the size of squares containing cross-triangle elements, see Figure 4. The largest relative increase in compliance used to determine the lower bound for the element size is

$$R = \max(R_1, R_2, R_3) \tag{30}$$

This value varies with α. Without losing generality in the following analysis, $\alpha = 1$ is assumed, yielding

$$R = \left(\frac{\eta_0\Delta_{\text{tc}}}{T_{\max}}\right)\frac{E'(\sqrt{2}+1)}{(1-\nu)h} \tag{31}$$

3.3. Bounds for element size

The two competing requirements for element size cannot be satisfied simultaneously for the exponential cohesive law of Xu and Needleman [9], cf. Reference [46]. However, for bilinear laws the analysis yields variable bounds since the finite initial stiffness of the cohesive surfaces (as measured by η_0 in a normalized sense) is an independent variable in the model.

First, the requirement that the finite element size is significantly smaller than the cohesive zone size yields

$$\frac{E\Phi_0}{hT_{\max}^2} \gg \frac{32(1-\nu^2)}{9\pi} \tag{32}$$

Here, Equation (21) has been used to approximate cohesive zone size.

Second, the requirement that $R \ll 1$ and Equation (31) yield

$$h \gg \left(\frac{\eta_0\Delta_{\text{tc}}}{T_{\max}}\right)\frac{E'(\sqrt{2}+1)}{(1-\nu)} \tag{33}$$

In order for Equations (32) and (33) to be simultaneously satisfied, $\eta_0 \ll 1$ is required. This condition imposes an upper limit on the initial stiffness of cohesive surfaces. The allowable range of element size can then be expressed as

$$\frac{9\pi E\Phi_0}{32(1-\nu^2)T_{\max}^2} \gg h \gg \left(\frac{\eta_0\Delta_{\mathrm{tc}}}{T_{\max}}\right)\frac{E'(\sqrt{2}+1)}{(1-\nu)} \tag{34}$$

These requirements should be enforced in a local sense for each element, ensuring satisfactory approximation of the system being analysed at any scale.

4. NUMERICAL CALCULATIONS AND DISCUSSIONS

Calculations are carried out to illustrate the application of Equation (34) and to develop a more accurate estimate of the bounds for the conditions (mesh triangulation, material systems and microstructural size scales) analysed in this paper. This numerical verification is also motivated by the fact that the cohesive zone size estimate in Equation (21) is based on a quasistatic solution and many CFEM simulations are dynamic. The calculations here use a range of element size and are carried out for a centre-cracked specimen under tensile loading. A homogeneous Al_2O_3 ceramic and a heterogeneous Al_2O_3/TiB_2 ceramic composite are chosen for the analysis. Figure 3 shows the specimen configuration used. One half of the specimen is used in the calculations due to symmetry. The whole specimen has a height of $2H = 1.6$ mm and a width of $2W = 1.6$ mm. The length of the initial crack is $2a_i = 0.4$ mm. The specimen is stress free and at rest initially. Tensile loading is applied by imposing symmetric velocity boundary conditions along the upper and lower edges of the specimen. Conditions of plain strain are assumed to prevail. The finite element mesh is shown in Figure 4. The small region in front of the crack tip contains very fine mesh in order to resolve the intensified stress field.

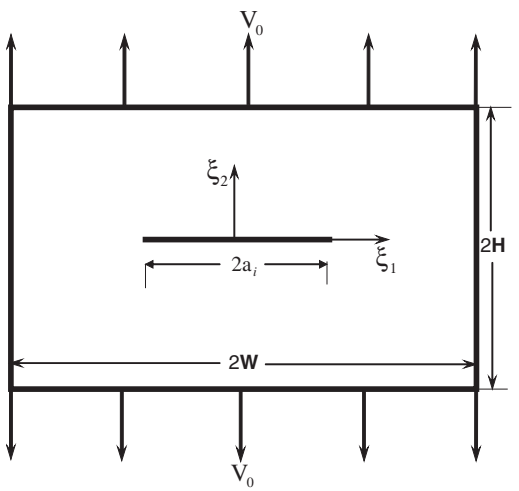

Figure 3. Specimen configuration for calculations.

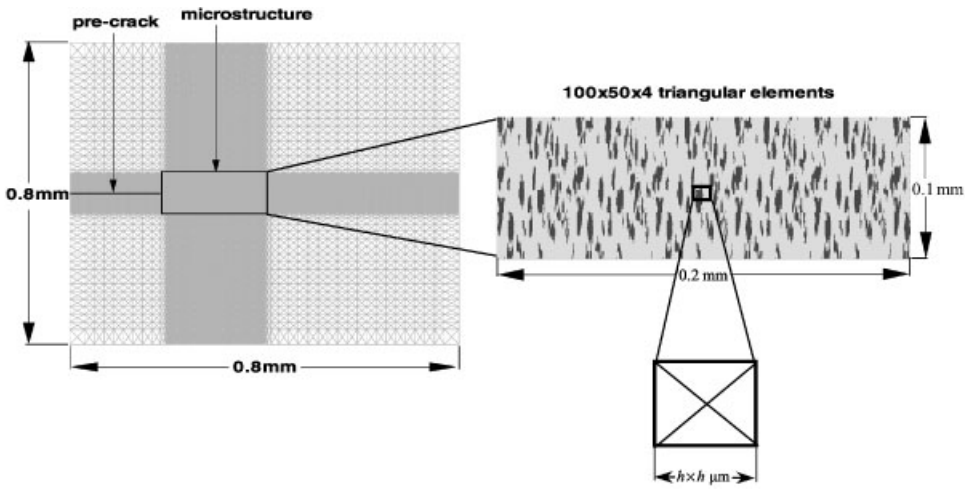

Figure 4. Finite element discretization.

Table I. Constitutive parameters for bulk and cohesive surfaces.

Compound	Density (kg/m^3)	K_{IC} ($Mpa\sqrt{m}$)	E (GPa)	ν	T_{max} (GPa)	Δ_{nc}, Δ_{tc} (nm)	Φ_0 (J/m^2)
Al_2O_3	3990	4.0	340	0.23	0.5	100	25
TiB_2	4520	7.2	500	0.12	1.0	100	50
Homogenized Al_2O_3/TiB_2 Composite	4120	3.6	415	0.15	0.65	100	32.5
Al_2O_3/TiB_2 Interface	—	—	—	—	0.5	100	25

In the case of the Al_2O_3/TiB_2 ceramic composite, this region represents the microstructure digitized from micrographs of actual materials. The two phases are identified and made different by their different material properties. Each element is either in Al_2O_3 or TiB_2. This numerical representation is obtained from digital micrographs of real materials which use photographic contrast to distinguish the phases. A uniform mesh is used in the simulations. For the smaller (TiB2 particles) phase, the average number of elements in each particle is approximately 25. The analyses carried out here are limited only to lengths of crack propagation within this microstructural region. The material outside the microstructure window is assumed to be homogeneous and assigned effective properties representative of those for the Al_2O_3 ceramic or the Al_2O_3/TiB_2 ceramic composite, see Table I. Both regions are discretized in the same manner, involving both bulk element and cohesive surface elements. For the results discussed here, the imposed boundary velocity of $V_0 = 2$ m/s is applied on top and bottom edges with a linear ramp from zero to this maximum velocity in the first 0.01 μs of loading. All other specimen surfaces have traction-free boundary conditions. Specifically, the loading

conditions are

$$\dot{u}_2(\xi_1, \pm H, t) = \begin{cases} \pm\dfrac{t}{0.01} V_0, & t < 0.01\ \mu\text{s} \\ \pm V_0 & t > 0.01\ \mu\text{s} \end{cases} \quad -W < \xi_1 < W$$

$$T^1(\xi_1, \pm H, t) = 0, \quad -W < \xi_1 < W \tag{35}$$

and

$$T^1(\pm W, \xi_2, , t) = T^2(\pm W, \xi_2, t) = 0, \quad -H < \xi_2 < H$$

This set of conditions represents the loading of the pre-crack by a tensile wave with stress amplitude of 16.5 MPa ($\rho c V_0$) and a linear ramp from zero to that value in 0.01 μs. The material properties in Table I are consistent with those in Reference [68]. These values for the cohesive energy per unit area (Φ_0) and the maximum cohesive traction ($T_{\max}$) allow Equation (34) to specialize to

$$32\ \mu\text{m} \gg h \gg 225\eta_0\ \mu\text{m} \tag{36}$$

for the Al_2O_3 ceramic and

$$29\ \mu\text{m} \gg h \gg 186\eta_0\ \mu\text{m} \tag{37}$$

for the Al_2O_3/TiB_2 composite. Note that the limits involved here are based on approximate analyses and are not exact. They can be specified more precisely through numerical simulations of individual structures with desired levels of tolerance for error. During the calculations, the time history of apparent crack length a (crack length projected on to the ξ_1-axis, Figure 3) is used as a measure for identifying the element size independence of solutions. Figure 5 shows contours of the Cauchy stress component σ_{22} in the Al_2O_3 ceramic and the Al_2O_3/TiB_2 composite at a time of $t = 0.12$ μs. These calculations are carried out with $h = 2$ μm and $\eta_0 = 0.001$ and are used to illustrate the types of the fracture processes we will deal with in this paper. In the case of the homogeneous Al_2O_3 (Figure 5a), the crack grows straight in the horizontal direction. The difference between the total crack (arc) length and the apparent crack length is insignificant. Consequently, the apparent crack length can be used a measure for quantifying the rate of solution convergence under different conditions. However, in the case of the Al_2O_3/TiB_2 composite (Figure 5b) crack path is not straight. Instead, the crack follows a zig-zag pattern along the interface between the TiB_2 particles and the Al_2O_3 matrix. Additionally, multiple crack fronts are active. A realistic quantification of solution convergence in this case should consider actual crack paths and stress fields. Therefore, our discussions below involve comparisons of stress fields and crack patterns as well as crack lengths in the case of the Al_2O_3/TiB_2 composite. In addition, the time history of total energy dissipated ($\phi = \int_{S_d} \Phi_d \, dS$, S_d being the total crack surface area) is also compared in all cases. As a practical measure, solution convergence is said to have occurred if the crack lengths and total energy dissipated from two successive calculations are within ±5% of each other over the duration deformation analysed.

Equations (36) and (37) show that the lower bound decreases as η_0 decreases. When $\eta_0 = 0$, the lower bound is 0; consequently, only the upper bound exists. For reasons discussed earlier,

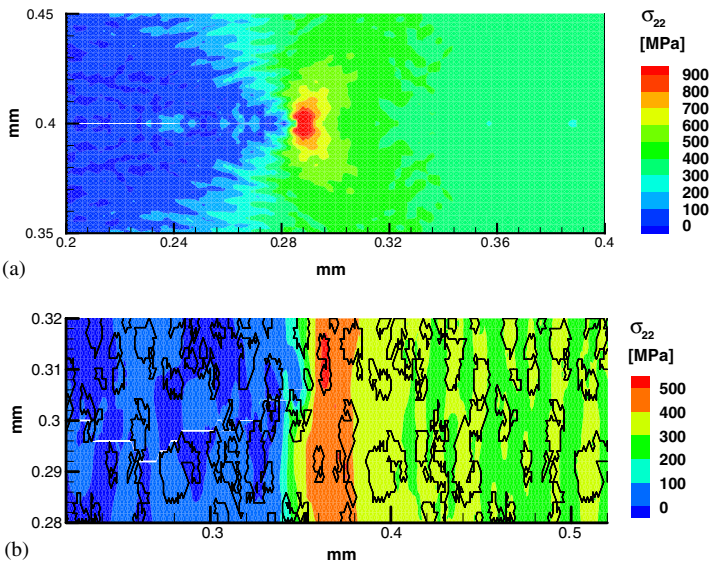

Figure 5. Crack formation and stress contours in: (a) Al_2O_3; and (b) Al_2O_3/TiB_2 at time $t = 0.12\,\mu s$.

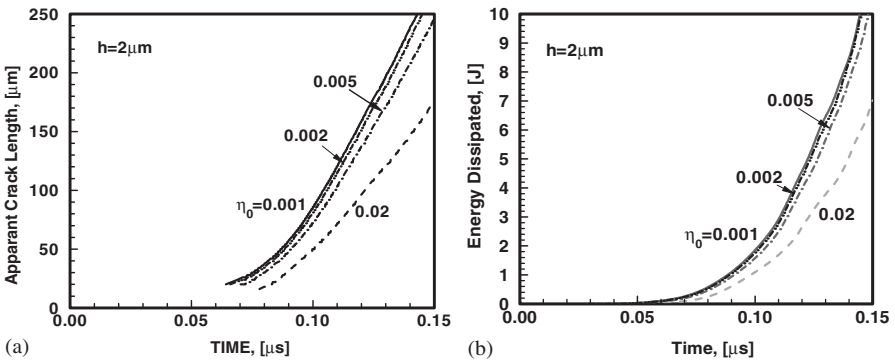

Figure 6. Time histories of: (a) apparent crack length; and (b) total energy dissipated for different values of stiffness parameter (Al_2O_3).

we avoid the use of initially rigid cohesive relations. To examine the effect of η_0 on solution convergence, calculations are carried out using a fixed element size of $h = 2\,\mu m$ for the homogeneous Al_2O_3. The results for four values of η_0 (0.02, 0.005, 0.002, and 0.001) are shown in Figure 6. Both the time of crack initiation and the growth of cracks are significantly influenced by the variation in η_0 (Figure 6(a)). A similar trend is observed for the energy dissipated in Figure 6(b). The solutions converge as η_0 decreases. The results for $\eta_0 \leqslant 0.002$ are quite close to each other, suggesting an empirical threshold for convergence. Based on this result, the lower bound for the element size in Equation (36) for the problem analysed can be

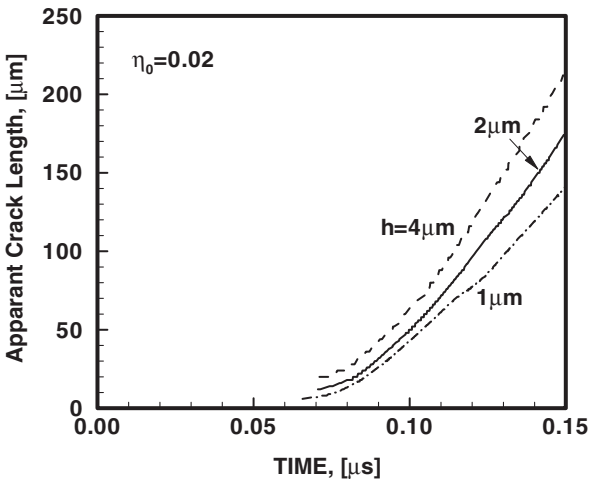

Figure 7. Time histories of apparent crack length for different element sizes (Al_2O_3).

more accurately stated as

$$d_z = 32 \gg h > 0.45\ \mu\text{m} \tag{38}$$

To further examine this issue, calculations with three different element sizes ($h = 1, 2$ and 4 μm) and $\eta_0 = 0.02$ are carried out. The results are shown in Figure 7. The solutions (as measured by the crack length history) diverge as h is decreased. The reason is clear: the lower bound for the mesh size given by Equation (36) is 4.5 μm in this case, higher than the mesh sizes actually used. This combination of material parameters and mesh design does not allow the conflicting requirements on mesh size embodied in Equation (36) to be satisfied simultaneous, directly causing the solution divergence seen. Figure 7 also shows that the crack initiation time increases and crack speed decreases with decreasing mesh sizes. This is because the increasing density of cohesive surfaces due to reduction in mesh size causes severe material softening that leads to lower wave speeds. Accordingly, the crack speed decreases. This is a direct consequence of the reduction in the overall stiffness of the model associated with mesh refinement.

Figure 8(a) shows the time histories of the apparent crack length for Al_2O_3 ceramic specimens with cohesive surfaces specified only along a straight line in front of the initial pre-crack. Four finite element sizes ($h = 2, 4, 8$ and 16 μm) are used for the region ahead of the crack tip with uniform elements. Clearly, the difference between the crack length histories becomes increasingly smaller as the element size is decreased, indicating solution convergence. This convergence occurs for finite element sizes in the range specified by Equation (38). Note that the lower bound of the finite element size is not specifically relevant for this figure since the specification of cohesive surfaces only along a constrained path does not lead to further stiffness reduction as the mesh is refined. In such cases, there is no effective lower limit on the mesh size. However, the results shown confirm relevance of the upper limit in Equation (34). Specifically, the results indicate that accurate resolution of the stress field in a cohesive zone is possible only if the element size is less than one-tenth of the size of the cohesive zone.

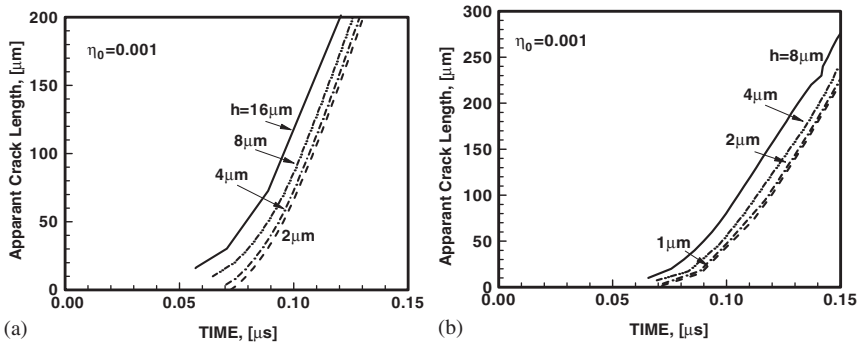

Figure 8. Time histories of crack length for Al_2O_3 with $\eta_0 = 0.001$: (a) case with cohesive elements only along the line in front of the initial crack tip; and (b) case with cohesive elements along all finite element boundaries.

In order to obtain a more accurate characterization of the upper bound, calculations are carried out for Al_2O_3 specimens with distributed cohesive surfaces. A stiffness parameter of $\eta_0 = 0.001$ and four finite element sizes ($h = 1$, 2, 4 and 8 μm) are used. Figure 8(b) shows the time histories of the apparent crack length for these element sizes. The solutions converge quickly as the element size is below one-tenth of the cohesive zone size ($h < 3$ μm), with the crack length histories for $h = 1$ and 2 μm nearly coinciding. Note that convergence is achieved here by keeping the element size well below the upper limit of 32 μm and above the lower limit of 0.45 μm specified in Equation (38). The results in Figures 8(a) and 8(b) allow the upper limit to be more accurately specified in an empirical manner for the conditions analysed. The tightened empirical range can be expressed as

$$0.1d_z \simeq 3\ \mu\text{m} > h > 0.45\ \mu\text{m} \tag{39}$$

Here, the upper bound is based on the observations from Figures 8(a) and 8(b). On the other hand, the lower bound comes directly from Equation (38).

Inhomogeneous and multiphase microstructures contain length scales that can affect solution convergence in CFEM calculations. The applicability of the above criterion should also be analysed in such a context. For example, the lower bound on element size is based on an energy argument which assumes homogeneous material properties. Although this does not represent a fundamental issue because the criterion can always be applied 'conservatively' for each locally homogeneous region, it is important to verify the usefulness of the criterion for heterogeneous materials. For this purpose, calculations are carried out for an Al_2O_3/TiB_2 ceramic composite system. A typical microstructure consisting of TiB_2 reinforcements in an Al_2O_3 matrix, cf. Reference [69], is obtained from a digitized micrograph of an actual material sample. To carry out the analysis, the interfacial bonding strength (or the maximum tensile strength in the cohesive law in Equation (11)) between the two phases is chosen to be the same as that for the matrix material. Interfacial and bulk parameters for the constituents are given Table I. Before the analysis can be carried out, we need to make sure that the microstructure window in Figure 4 contains a sufficiently large microstructural sample for resolving the fracture process over the duration of interest without significant edge effect. For this purpose, two different

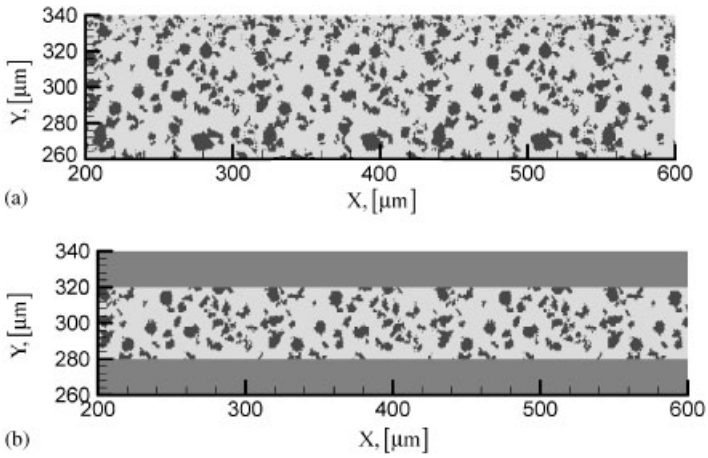

Figure 9. Two different microstructural window sizes: (a) $80 \times 400\,\mu m$; and (b) $40 \times 400\,\mu m$.

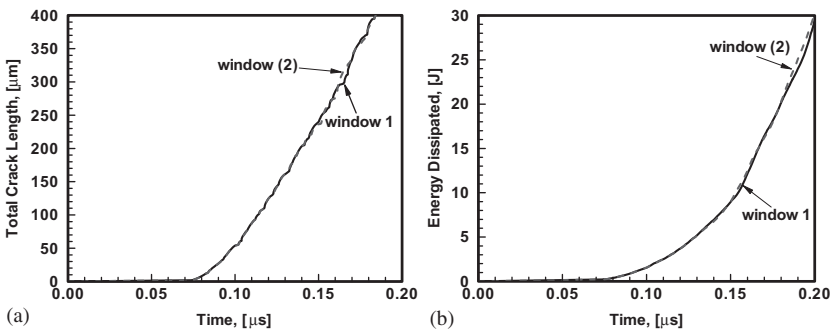

Figure 10. Time histories of: (a) total crack length; and (b) total energy dissipated for two different microstructural window sizes (Al_2O_3/TiB_2).

window sizes (see Figure 9) are used. In both cases, $h = 2\,\mu m$ and $\eta_0 = 0.001$, allowing the conditions of Equation (39) to be satisfied. Figure 10 shows the time histories of total crack length and energy dissipated for the two cases. The results are essentially the same, suggesting that either sample size is sufficient for resolving the fracture process over the time duration analysed. Based on this result, all calculations here and in References [59, 60] are carried out with the smaller window size.

To verify the applicability of the criterion to heterogeneous materials, four values of η_0 (0.1, 0.03, 0.01, and 0.005) are considered along with $h = 2\,\mu m$. The results in Figure 11(a) show that the time history of apparent crack length starts to converge as η_0 approaches 0.005. To further analyse the issue, calculations are also carried out for $h = 1$ and $2\,\mu m$, with $\eta_0 = 0.001$. The near coincidence of the apparent crack length histories in Figure 11(b) indicates convergence of the solutions. This convergence is more clearly seen in the crack paths and stress contours from these two calculations shown in Figure 12. Clearly, not only the crack

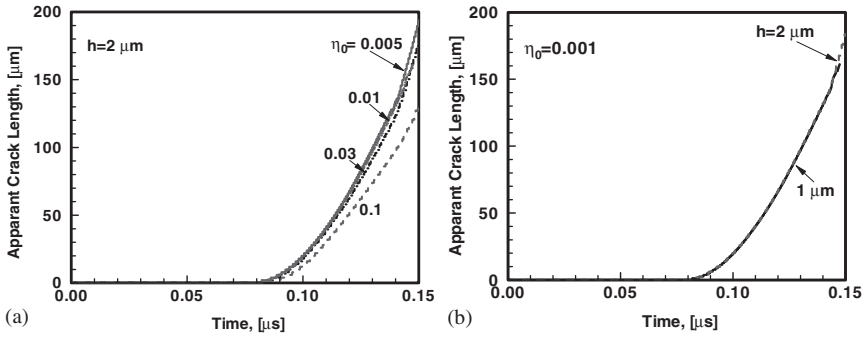

Figure 11. Apparent crack length histories in Al_2O_3/TiB_2 microstructures: (a) results for different η_0 values with $h = 2\,\mu m$; and (b) results for different h values with $\eta_0 = 0.001$.

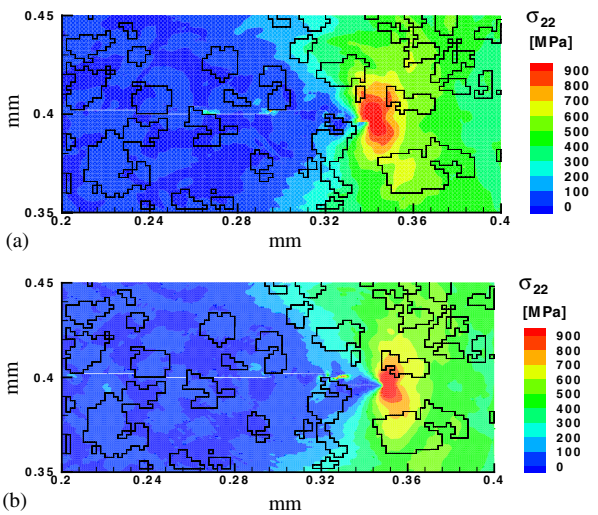

Figure 12. Stress contours and crack patterns in Al_2O_3/TiB_2 microstructures with $\eta_0 = 0.001$ at time $t = 0.12\,\mu s$: (a) $h = 2\,\mu m$; and (b) $h = 1\,\mu m$.

paths are nearly identical, the contours of σ_{22} also closely resemble each other. The results here confirm the applicability of the criterion in Equation (39) to inhomogeneous materials with microstructures as well.

Finally, we close by pointing out that calculations using several real microstructures of the Al_2O_3/TiB_2 composite system have been carried out under various conditions. The results have allowed the effects of phase arrangement, phase morphology, and phase size scale to be analysed and quantified. More details of the analyses and results are given in Reference [59].

5. CONCLUDING REMARKS

An analysis of the factors influencing solution convergence in a CFEM model with bilinear variable stiffness cohesive surfaces has been carried out. In the formulation, the initial stiffness is an independent variable of the model. As a result of the analysis and calculations, the following points can be highlighted.

1. Factors setting length scales and requiring sufficiently small element sizes for solution convergence include cohesive zone size and characteristic microstructural dimensions. First-order approximations of the cohesive zone size have been used to obtain an upper bound of allowable finite element sizes, consistent with what has been analysed in the literature;
2. A lower bound for element size in two-dimensional CFEM models with cross triangular elements has been obtained to limit changes in model response due to stiffness reduction associated with the specification of cohesive surfaces in a distributed manner. Both the upper bound and the lower bound are given as functions of bulk and interfacial properties of relevant materials;
3. Calculations are carried out under conditions of plane strain and uniform meshes with cross-triangle elements. The results are used to empirically refine the upper and lower bounds for models with Al_2O_3 or Al_2O_3/TiB_2 material properties.
4. Although a specific mesh design and a hyperelastic material constitutive characterization are involved here, the framework of analysis, the parametric dependence, and the general trends revealed by the criterion developed here should be a useful guide for choice of element size for CFEM models with other element design and constitutive characterizations as well. Accurate specifications of the limits under differing conditions can be obtained in a manner similar to what is employed here.

APPENDIX A: EFFECTIVE MODULI OF CFEM MODELS WITH CROSS-TRIANGLE ELEMENTS

Case I (*Uniform uniaxial tension*): Suppose that the discretized CFEM system and its equivalent homogeneous system are both subjected to uniform uniaxial tensile loading under stress σ_0 in the x-direction. We calculate the effective Young's modulus for the discrete system E_{eff} via an equivalent strain energy method by equating the discrete system's strain energy to that of the equivalent homogeneous system. The representative volume we choose should consist of a sufficient (and variable) number of elements. We assume the part of the discrete system analysed consists of $N \times M$ unit rectangles and each rectangle contains 4 cross-triangular elements. Here, N and M are variable. Obviously, the total potential energy stored in the discrete system is the sum of the strain energy stored in all the bulk elements and the cohesive energy stored in the cohesive surfaces, i.e.

$$U^{(1)} = U_{\text{b}}^{(1)} + U_{\text{c}}^{(1)} \tag{A1}$$

Under uniform tensile loading with σ_0, the only nontrivial stress component in the bulk elements is $\sigma_{xx} = \sigma_0$. Simple derivations yield

$$U_{\text{b}}^{(1)} = N \times M \times h^2 \times \frac{1}{2} \frac{\sigma_0^2}{E'}$$

and

$$U_{\mathrm{c}}^{(1)} = N \times M \times h \times \left[2 \times \sqrt{2} \times \frac{(\sigma_0/2)^2}{2} \frac{\eta_0 \Delta_{\mathrm{tc}}}{\alpha T_{\max}} + 2 \times \sqrt{2} \times \frac{(\sigma_0/2)^2}{2} \frac{\eta_0 \Delta_{\mathrm{nc}}}{T_{\max}} + \frac{\sigma_0^2}{2} \frac{\eta_0 \Delta_{\mathrm{nc}}}{T_{\max}} \right]$$

$$= N \times M \times h \times \frac{1}{2} \sigma_0^2 \left[\left(\frac{\sqrt{2}+2}{2} \right) \frac{\eta_0 \Delta_{\mathrm{nc}}}{T_{\max}} + \frac{\sqrt{2}}{2} \frac{\eta_0 \Delta_{\mathrm{tc}}}{\alpha T_{\max}} \right] \tag{A2}$$

The potential energy for the equivalent homogeneous system is

$$U^{(2)} = N \times M \times h^2 \times \frac{1}{2} \frac{\sigma_0^2}{E_{\mathrm{eff}}} \tag{A3}$$

Requiring that

$$U^{(1)} = U_{\mathrm{b}}^{(1)} + U_{\mathrm{c}}^{(1)} = U^{(2)} \tag{A4}$$

we obtain

$$\frac{1}{E_{\mathrm{eff}}} = \frac{1}{E'} + \frac{1}{h} \left[\left(\frac{\sqrt{2}+2}{2} \right) \frac{\eta_0 \Delta_{\mathrm{nc}}}{T_{\max}} + \frac{\sqrt{2}}{2} \frac{\eta_0 \Delta_{\mathrm{tc}}}{\alpha T_{\max}} \right] \tag{A5}$$

Case II (*Biaxial uniform tension*): This case involves uniform biaxial tensile loading with intensity σ_0 in both x- and y-directions. The block is under a two-dimensional hydrostatic loading with $\sigma_{xx} = \sigma_{yy} = \sigma_0$. The potential energy of discrete system is

$$U^{(1)} = U_{\mathrm{b}}^{(1)} + U_{\mathrm{c}}^{(1)} \tag{A6}$$

where

$$U_{\mathrm{b}}^{(1)} = N \times M \times h^2 \times \frac{\sigma_0^2}{E'} (1 - \nu)$$

and

$$U_{\mathrm{c}}^{(1)} = N \times M \times h \times \left[2 \times \sqrt{2} \times \frac{\sigma_0^2}{2} \left(\frac{\eta_0 \Delta_{\mathrm{tc}}}{\alpha T_{\max}} \right) + 2 \times \frac{\sigma_0^2}{2} \left(\frac{\eta_0 \Delta_{\mathrm{nc}}}{T_{\max}} \right) \right]$$

$$= N \times M \times h \times \sigma_0^2 \left[\sqrt{2} \left(\frac{\eta_0 \Delta_{\mathrm{tc}}}{\alpha T_{\max}} \right) + \left(\frac{\eta_0 \Delta_{\mathrm{nc}}}{T_{\max}} \right) \right] \tag{A7}$$

The potential energy for the equivalent homogeneous system is

$$U^{(2)} = N \times M \times h^2 \times \frac{\sigma_0^2}{E_{\mathrm{eff}}} (1 - \nu_{\mathrm{eff}}) \tag{A8}$$

The requirement that $U^{(1)} = U_{\mathrm{b}}^{(1)} + U_{\mathrm{c}}^{(1)} = U^{(2)}$ yields

$$\frac{1-v_{\mathrm{eff}}}{E_{\mathrm{eff}}} = \frac{1-v}{E'} + \frac{1}{h}\left[\sqrt{2}\left(\frac{\eta_0\Delta_{\mathrm{tc}}}{\alpha T_{\max}}\right) + \left(\frac{\eta_0\Delta_{\mathrm{nc}}}{T_{\max}}\right)\right] \tag{A9}$$

One can solve for v_{eff} by substituting (A5) into the above equation.

Case III (*Pure shear*): Under conditions of loading with a uniform pure shear traction on the surfaces, the potential energy of the discrete system is

$$U^{(1)} = U_{\mathrm{b}}^{(1)} + U_{\mathrm{c}}^{(1)} \tag{A10}$$

where

$$U_{\mathrm{b}}^{(1)} = N \times M \times h^2 \times \frac{\sigma_0^2}{2G}$$

and

$$\begin{aligned} U_{\mathrm{c}}^{(1)} &= N \times M \times h \times \left[2 \times \frac{\sigma_0^2}{2}\left(\frac{\eta_0\Delta_{\mathrm{tc}}}{\alpha T_{\max}}\right) + 2 \times \sqrt{2} \times \frac{\sigma_0^2}{2}\left(\frac{\eta_0\Delta_{\mathrm{nc}}}{T_{\max}}\right)\right] \\ &= N \times M \times h \times \sigma_0^2\left[\left(\frac{\eta_0\Delta_{\mathrm{tc}}}{\alpha T_{\max}}\right) + \sqrt{2}\left(\frac{\eta_0\Delta_{\mathrm{nc}}}{T_{\max}}\right)\right] \end{aligned} \tag{A11}$$

The potential energy for the equivalent homogeneous system is

$$U^{(2)} = N \times M \times h^2 \times \frac{\sigma_0^2}{2G_{\mathrm{eff}}} \tag{A12}$$

Again, the requirement that $U^{(1)} = U_{\mathrm{b}}^{(1)} + U_{\mathrm{c}}^{(1)} = U^{(2)}$ yields

$$\frac{1}{G_{\mathrm{eff}}} = \frac{1}{G} + \frac{1}{h}\left[2\left(\frac{\eta_0\Delta_{\mathrm{tc}}}{\alpha T_{\max}}\right) + 2\sqrt{2}\left(\frac{\eta_0\Delta_{\mathrm{nc}}}{T_{\max}}\right)\right] \tag{A13}$$

Thus, all three effective parameters have been obtained as functions of constants for the bulk material and the cohesive surfaces.

ACKNOWLEDGEMENTS

The support from the Army Research Office through Grant No. DAAG55-98-1-0454 and the National Science Foundation through CAREER Grant No. CMS9984298 is gratefully acknowledged. Calculations reported are carried out on the Cray Computers at the San Diego Supercomputer Center, Jet Propulsion Laboratory and Naval Oceanographic Office Major Shared Resource Center.

REFERENCES

1. Barenblatt GI. The mathematical theory of equilibrium of cracks in brittle fracture. *Advances in Applied Mechanics* 1962; **7**:55–129.

2. Dugdale DS. Yielding of steel sheets containing slits. *Journal of the Mechanics and Physics of Solids* 1960; **8**:100–104.
3. Needleman A. A continuum model for void nucleation by inclusion debonding. *Journal of Applied Mechanics* 1987; **38**:289–324.
4. Tvergaard V. Effect of fiber debonding in a whisker-reinforced material. *Material Science and Engineering* 1990; **A125**:203–213.
5. Shabrov MN, Needleman A. An analysis of inclusion morphology effects on void nucleation. *Modeling and Simulation in Material Science and Engineering* 2002; **10**:163–183.
6. Needleman A. An analysis of decohesion along an imperfect interface. *International Journal of Fracture* 1990; **42**:21–40.
7. Needleman A. Analysis of tensile decohesion along an interface. *Journal of the Mechanics and Physics of Solids* 1990; **38**:289–324.
8. Tvergaard V, Hutchinson JW. The relation between crack growth and fracture process parameters in elastic–plastic solids. *Journal of the Mechanics and Physics of Solids* 1992; **40**:1377–1397.
9. Xu XP, Needleman A. Numerical simulations of fast crack growth in brittle solids. *Journal of the Mechanics and Physics of Solids* 1994; **42**:1397–1434.
10. Pandolfi A, Guduru PR, Ortiz M, Rosakis AJ. Three dimensional cohesive-element analysis and experiments of dynamic fracture in C300 steel. *International Journal of Solids and Structures* 2000; **37**(27):3733–3760.
11. Ruiz G, Pandolfi A, Ortiz M. Three-dimensional cohesive modeling of dynamic mixed-mode fracture. *International Journal for Numerical Methods in Engineering* 2001; **52**:97–120.
12. Xu XP, Needleman A. Numerical simulations of dynamic interfacial crack growth allowing for crack growth away from the bond line. *International Journal of Fracture* 1995; **74**:253–275.
13. Xu XP, Needleman A. Numerical simulations of dynamic crack growth along an interface. *International Journal of Fracture* 1996; **74**:289–324.
14. Siegmund T, Needleman A. A numerical study of dynamic crack growth in elastic–viscoplastic solids. *International Journal of Solids and Structures* 1997; **34**:769–787.
15. Rosakis AJ, Samudrala O, Singh RP, Shukla A. Intersonic crack propagation in bimaterials. *Journal of the Mechanics and Physics of Solids-Special Volume on Dynamic Deformation and Failure Mechanics of Materials* 1998; **46**:1789–1813.
16. Camacho GT, Ortiz M. Computational modeling of impact damage in brittle materials. *International Journal of Solids and Structures* 1996; **33**:2899–2938.
17. Miller O, Freund LB, Needleman A. Modeling and simulation of dynamic fragmentation in brittle materials. *International Journal of Fracture* 1999; **96**(2):101–125.
18. Espinosa H, Zavattieri P, Dwivedi SK. A finite deformation continuum/discrete model for the description of fragmentation and damage in brittle materials. *Journal of the Mechanics and Physics of Solids* 1998; **46**(10):1909–1942.
19. Espinosa H, Zavattieri P, Emore G. Adaptive FEM computation of geometrical and material nonlinearities with application to brittle materials. *Mechanics of Materials* 1998; **29**:275–305.
20. Zhai J, Zhou M. Micromechanical modeling of mixed-mode crack growth in ceramic composites. In *Mixed Mode Crack Behavior*, Miller K, McDowell DL (eds). ASTM: Philadelphia, 1999; 174–200.
21. Zhai J, Zhou M. Finite element analysis of micromechanical failure modes in heterogeneous brittle solids. *International Journal of Fracture*, *Special Issue on Failure Mode Transition in Solids* 2000; **101**:161–180.
22. Geubelle P, Baylor J. Impact-induced delamination of composites: a 2-D simulation. *Composites Part B*: *Engineering* 1998; **29**:589–602.
23. Minnaar K, Zhou M. Real-time detection and explicit finite element simulation of delamination in composite laminates under impact loading. In *AMD ASME IMECE*, Orlando, FL, USA, 2000; 67–78.
24. Minnaar K, Zhou M. Experimental characterization and numerical simulation of impact damage in composite laminates. In *ASME IMECE*, New York, 2001.
25. Espinosa HD, Dwivedi S, Lu H-C. Modeling impact induced delamination of woven fiber reinforced composites with contact/cohesive laws. *Computer Methods in Applied Mechanics and Engineering* 2000; **183**:259–290.
26. Zou Z, Reid SR, Li S. A continuum damage model for delamination in laminated composites. *Journal of the Mechanics and Physics of Solids* 2003; **51**:333–356.
27. Xuan W, Curtin WA, Needleman A. Stochastic microcrack nucleation in lamellar solids. *Engineering Fracture Mechanics* 2003; **70**:1869–1884.

28. Rahul-Kumar P, Jagota A, Bennison SJ, Saigal S, Muralidhar S. Polymer interfacial fracture simulations using cohesive elements. *Acta Materialia* 1999; **47**(15–16):4161–4169.
29. Rahul-Kumar P, Jagota A, Bennison SJ, Saigal S, Muralidhar S. Cohesive element modeling of viscoelastic fracture: application to peel testing of polymers. *International Journal of Solids and Structures* 2000; **37**(13): 1873–1897.
30. Rahul-Kumar P, Jagota A, Bennison SJ, Saigal S, Muralidhar S. Interfacial failures in a compressive shear strength test of glass/polymer laminates. *International Journal of Solids and Structures* 2000; **37**(48–50): 7281–7305.
31. Roychowdhury S, Arun Roy YD, Dodds J, Robert H. Ductile tearing in thin aluminum panels: experiments and analyses using large-displacement, 3-D surface cohesive elements. *Engineering Fracture Mechanics* 2002; **69**(8):983–1002.
32. Zavattieri PD, Raghuram PV, Espinosa HD. A computational model of ceramic microstructures subjected to multi-axial dynamic loading. *Journal of the Mechanics and Physics of Solids* 2001; **49**:27–68.
33. Scheider I, Brocks W. Simulation of cup-cone fracture using the cohesive model. *Engineering Fracture Mechanics* 2003; **70**:1943–1961.
34. Gomez FJ, Elices M. Fracture of components with V-shaped notches. *Engineering Fracture Mechanics* 2003; **70**:1913–1927.
35. Yuan H, Chen J. Computational analysis of thin coating layer failure using a cohesive model and gradient plasticity. *Engineering Fracture Mechanics* 2003; **70**:1929–1942.
36. Jin Z-H, Paulino GH, Dodds RH Jr. Cohesive fracture modeling of elastic–plastic crack growth in functionally graded materials. *Engineering Fracture Mechanics* 2003; **70**:1885–1912.
37. Carpinteri A, Cornetti P, Barpi F, Valente S. Cohesive crack model crack description of ductile to brittle size-scale transition: dimensional analysis vs. renormalization group theory. *Engineering Fracture Mechanics* 2003; **70**:1809–1839.
38. Gao H, Klein P. Numerical simulation of crack growth in an isotropic solid with randomized cohesive bonds. *Journal of the Mechanics and Physics of Solids* 1998; **46**:187–218.
39. Gao H, Baohua J. Modeling fracture in nanomaterials via a virtual internal bond method. *Engineering Fracture Mechanics* 2003; **70**:1777–1791.
40. de Borst R. Numerical aspects of cohesive zone models. *Engineering Fracture Mechanics* 2003; **70**: 1743–1757.
41. Planas J, Elices M, Guinea GV, Goemez FJ, Cendon DA, Arbilla I. Generalizations and specializations of cohesive crack models. *Engineering Fracture Mechanics* 2003; **70**:1759–1776.
42. Pandolfi A, Yu C, Corigliano A, Ortiz M. Modeling dynamic fracture in transversely isotropic composites: a cohesive approach. California Institute of Technology, Caltech, 2000. ASCI/2000.097.
43. Yu C, Pandolfi A, Ortiz M, Coker D, Rosakis AJ. Three-dimensional modeling of intersonic shear-crack growth in asymmetrically loaded unidirectional composite plates. *International Journal of Solids and Structures* 2002; **39**:6135–6157.
44. Pandolfi A, Ortiz M. An efficient adaptive procedure for three-dimensional fragmentation simulations. *Engineering Computations* 2002; **18**:148–159.
45. Tijssens M. On the cohesive surface methodology for fracture of brittle heterogeneous solids. *Ph.D. Thesis*, Technical University Delft, 2000.
46. Falk MA, Needleman A, Rice JR. A critical evaluation of dynamic fracture simulations using cohesive surfaces. *Journal de Physique IV* 2001; **11**:43–52.
47. Ortiz M, Pandolfi A. Finite deformation irreversible cohesive elements for three dimensional crack-propagation analysis. *International Journal for Numerical Methods in Engineering* 1999; **44**(9):1267–1282.
48. Carpinteri JA, Chiaia B, Cornetti P. A scale-invariant cohesive crack model for quasi-brittle materials. *Engineering Fracture Mechanics* 2002; **69**:207–217.
49. Spearot DE, Jacob KI, McDowell DL. Nonlocal separation constitutive laws for interfaces and their relation to nanoscale simulations. *Mechanics of Materials* 2004; **36**(9):825–847.
50. Prado EP, van Mier JGM. Effect of particle structure on model-I fracture process in concrete. *Engineering Fracture Mechanics* 2003; **70**:1793–1807.
51. Sorensen BF, Jacobsen TK. Determination of cohesive laws by the J integral approach. *Engineering Fracture Mechanics* 2003; **70**:1841–1858.
52. Nguyen O, Ortiz M. Coarse-graining and renormalization of atomistic binding relations and universal macroscopic cohesive behaviour. *Journal of the Mechanics and Physics of Solids* 2002; **50**(8):1727–1741.

53. Papoulia KD, Vavasis SA. Time-continuous cohesive interface finite elements in explicit dynamics. In *15th ASCE Engineering Mechanics Conference*. Columbia University, New York, NY, 2002.
54. Klein P, Foulk J, Chen E, Wimmer S, Gao H. Physics-based modeling of brittle fracture: cohesive formulations and the application od meshfree methods. Sandia National Laboratories, USA, 2000. SAND2001-8099.
55. Shet C, Chandra N. Analysis of energy balance when using cohesive zone models to simulate fracture processes. *Journal of Engineering Materials and Technology* 2002; **124**:440–450.
56. Minnaar K. Experimental and numerical analysis of damage in laminate composites under low velocity impact loading. *Ph.D. Thesis*, Georgia Institute of Technology, Atlanta, GA, 2002.
57. Cornec A, Scheider I, Schwalbe K-H. On the practical application of the cohesive zone model. *Engineering Fracture Mechanics* 2003; **70**:1963–1987.
58. Lin YK. *Probabilistic Theory of Structural Dynamics*. McGraw-Hill: New York, 1967.
59. Zhai J, Tomar V, Zhou M. Micromechanical modeling of dynamic fracture using the cohesive finite element method. *Journal of Engineering Materials and Technology* 2004; **126**:182–191.
60. Tomar V, Zhou M. Deterministic and stochastic analyses of fracture processes in a brittle microstructure system. *Engineering Fracture Mechanics* 2004, submitted.
61. Nguyen O, Repetto EA, Ortiz M, Radovitzky RA. A cohesive model of fatigue crack growth. *International Journal of Fracture* 2001; **110**:351–369.
62. Krieg RD, Key SW. Transient shell response by numerical integration. *International Journal for Numerical Methods in Engineering* 1973; **7**:273–286.
63. Belytschko T, Chiapetta RL, Bartel HD. Efficient large scale non-linear transient analysis by finite elements. *International Journal for Numerical Methods in Engineering* 1976; **10**:579–596.
64. Rice JR. Mathematical analysis in the mechanics of fracture. In *Fracture*, Liebowitz H (ed.), vol. 2. Academic Press: New York, 1968; 191–311.
65. Planas J, Elices M. Asymptotic analysis of a cohesive crack: 1. Theoretical background. *International Journal of Fracture* 1992; **55**:153–177.
66. Rice JR. The mechanics of earthquake rupture. In *Physics of the Earth's Interior*. Italian Physical Society: Italy, North-Holland Publ. Co.: Amsterdam, 1980; 555–649.
67. Xu XP, Needleman A, Abraham FF. Effect of inhomogeneities on dynamic crack growth in an elastic solid. *Modeling and Simulation in Material Science and Engineering* 1997; **5**:489–516.
68. Keller AR, Zhou M. Effect of microstructure on dynamic failure resistance of TiB_2/Al_2O_3 ceramics. *Journal of the American Ceramic Society* 2003; **86**(3):449–457.
69. Logan KV. Composite ceramics. *Final Technical Report*. USSTACOM DAAEO7-95-C-R040. 1996.

